Available online at www.sciencedirect.com

ScienceDirect

Polymer 49 (2008) 2133−2145

polymer

www.elsevier.com/locate/polymer

Structural changes during deformation in carbon nanotube-reinforced polyacrylonitrile fibers

Wenjie Wang [a], N. Sanjeeva Murthy [b,*], Han Gi Chae [c], Satish Kumar [c]

[a] Department of Physics, University of Vermont, Burlington, VT 05403, United States
[b] New Jersey Center for Biomaterials, Rutgers University, 145 Bevier Road, Piscataway, NJ 08854, United States
[c] School of Polymer, Textile and Fiber Engineering, Georgia Institute of Technology, Atlanta, GA 30332, United States

Received 27 October 2007; received in revised form 12 February 2008; accepted 16 February 2008
Available online 23 February 2008

Abstract

Structural changes during deformation in solution- and gel-spun polyacrylonitrile (PAN) fibers prepared with multi- and single-wall carbon nanotubes, and vapor-grown carbon nano-fibers were investigated using synchrotron X-ray diffraction data. Deformation of carbon nanotubes (CNTs) contributes to the increased modulus. CNTs, in addition to their mere presence as reinforcement, were found to alter the response of the PAN matrix to stress and thus enhance the performance of the composite. CNTs facilitate the orientation of the PAN crystals during deformation, and increase the load transferred to PAN crystals as evidenced by their increased lateral and axial strains at 75 °C. The monotonical decrease in PAN interchain spacing with the fiber strain was accompanied by a reversible helix to zigzag conformational change as well as by changes in the axial repeats of the two conformations. These changes were much larger in gel-spun fibers than in solution-spun fibers, indicating more effective load transfer in gel-spun fibers.

Keywords: Polyacrylonitrile; Nanocomposites; Deformation

1. Introduction

Polyacrylonitrile (PAN) fiber has been commercially available for decades, most significantly as a precursor of high-quality carbon fiber. As a part of the general effort to develop nano-reinforced materials with enhanced properties, recently there have been attempts to incorporate carbon nanotubes into PAN to enhance its mechanical, thermal and electrical properties [1−7]. To understand the underpinnings for such a property enhancement, knowledge of the structural changes in matrix, inclusions and the interphase between the two are necessary. A number of papers have been published on the structure of PAN using X-ray diffraction (XRD) [8−11], infrared spectroscopy [10], nuclear magnetic resonance (NMR) [12], and molecular simulations [13−15]. Based on the scattering pattern, PAN is considered either orthorhombic with 3D order [11,16], or hexagonal with 2D order [17]. It has been proposed that hexagonal packing of PAN chains in dry samples becomes orthorhombic due to co-crystallization of PAN with polar solvent molecules [18]. In this study, we use in situ XRD measurements, and draw upon these earlier publications, to understand the deformation process on microscopic scale in PAN and its nanocomposites. Experiments were peformed at various temperatures, below and above T_g, on PAN and its nanocomposites with single-wall nanotubes (PAN/SWNT), multi-wall carbon nanotubes (PAN/MWNT) and vapor-grown carbon nano-fibers (PAN/VGCNF).

2. Experimental

2.1. Materials

PAN and composite fibers prepared by conventional solution spinning and gel spinning with various nanotubes were

---

* Corresponding author. Tel.: +1 732 445 0488; fax: +1 732 445 5006.
E-mail address: murthy@biology.rutgers.edu (N.S. Murthy).

0032-3861/$ - see front matter © 2008 Elsevier Ltd. All rights reserved.
doi:10.1016/j.polymer.2008.02.035

described in our previous papers [2,19]. For conventional solution spinning, PAN (molecular weight 100,000 g/mol; 6.7% methylacrylate comonomer) was vacuum dried at 90 °C. Optically homogenous dispersion of carbon nanotubes (CNTs) in dimethyl acetamide (DMAc) was prepared by sonication (Branson 3510R-MT, 100 W, 42 kHz) and the CNT/DMAc dispersion was combined with PAN/DMAc solution. The solid concentration (polymer + CNT) was 17.5 wt%, and CNT concentration with respect to polymer was 5 wt%. Fibers were spun at room temperature by dry-jet-wet spinning. Final draw ratio for control PAN and composite fibers was 10. For gel spinning, PAN (molecular weight 250,000 g/mol; 6.5% methylacrylate comonomer) was used with SWNT. SWNT was dispersed in *N*,*N*-dimethylformamide (DMF) using bath type sonicator at 40 mg/L concentration. PAN was dissolved in DMF separately. After 24 h sonication of SWNT/DMF, this solution was added to PAN/DMF solution, and the excess amount of DMF was evaporated to obtain the desired solid concentration (13.7 wt%). SWNT concentration was set to be 1 wt% with respect to PAN. Subsequently, fibers were spun into cold methanol bath (approximately −50 °C) to generate gel fibers. After up to 7 days of gelation, the gel fibers were drawn in glycerol bath (~160 °C) to achieve a total draw ratio of 51. All the drawn fibers were dried at constant length in a vacuum oven at 50 °C. Table 1 lists the properties of both the dry-jet-wet-spun and gel-spun fibers.

2.2. Methods

Preliminary XRD data were collected on filament bundles using an in-house X-ray facility consisting of a Rigaku rotating anode, copper target, point collimation and a Bruker Highstar 2D detector. Extensive XRD data were collected at the Argonne Photon Source (APS) on the DND-CAT beam line 5ID-D using X-rays of wavelength 0.1 nm. Single filaments were attached to a cardboard tab (Miami Valley Gasket, Dayton, Ohio). Fibers (gauge length = 1 in.) were held perpendicular to the incident X-ray beam while being stretched to failure (except when exploring reversibility) in an Instron at a constant elongation rate, which was chosen so as to get sufficient number of X-ray frames prior to fiber breakage, the results being insensitive to these small changes in quasi-static strain rate: PAN – 0.033 in./min at room temperature, 0.04 in./min at 75 °C, and 0.03 in./min at 125 °C; PAN/MWNT – 0.053 in./min at room temperature, 0.04 in./min at 75 °C, and 0.05 in./min at 125 °C; PAN/VGCNF – 0.04 in./min at room temperature, 0.04 in./min at 75 °C and 0.04 in./min at 125 °C; Gel PAN/SWNT and Gel PAN – 0.021 in./min at room temperature and 0.03 in./min at 75 °C. XRD patterns were recorded as the fiber was stretched continuously in the Instron, and the load-elongation curves were recorded simultaneously. Data were collected for 9 s with gel-spun fibers at room temperature and 5 s for all other measurements, and 1 s was allowed for data transfer after each frame. We also obtained XRD data as the fibers were stretched at three pre-selected temperatures, ambient (22 °C), below T_g (~75 °C), and above T_g (~125 °C). Temperature was measured by placing a thermocouple right next to the specimen. The fiber was heated by a stream of hot air whose temperature was continuously monitored by a separate thermocouple and electronically controlled.

Uniaxial tensile test data were recorded continuously in the form of relative displacement of the two grips as function of time. The breakage of the fiber was signified by a sudden decrease in load. Strain is calculated as a mean of the values over 10 s or 6 s (9 s for imaging gel-spun fibers at room temperature and 5 s for all others, respectively; 1 s more for data acquisition), the interval between successive X-ray frames. In this paper, the term fiber strain, or strain, means the strain calculated for the filament as a whole from the Instron data. The terms lateral strain and axial strain refer to the X-ray or crystal strain calculated from XRD data, and correspond to the deformation of the unit cell of the PAN crystals in the equatorial and meridional directions, respectively.

Typical load–strain plots obtained at different temperatures are illustrated in Fig. 1. These data, which are obtained from single filaments, are reliable for solution-spun fibers (70–80 μm). But, the data, especially the moduli, are not accurate for the much thinner (~20 μm) gel-spun fibers. The structural change during elongation was followed by analyzing the wide-angle X-ray diffraction (WAXD) scans obtained at regular time intervals; each point in Fig. 1 and other plots correspond to one XRD pattern. Typical 2D WAXD patterns are shown in Fig. 2. Two complete sets of measurements were carried out, and we present only the second set of data. The first set was consistent with the second one.

2.3. Analysis

Data were analyzed using codes written in MATLAB. 2D patterns were converted into three categories of 1D scans, equatorial, meridional and azimuthal. To obtain 1D equatorial and meridional scans, the intensities were sector-averaged such that the intensity at each 2θ (scattering angle) is an

Table 1
Fiber diameter and mechanical properties

		Diameter (μm)	Tensile modulus (GPa)	Tensile strength (GPa)	Elongation at break (%)
Conventional solution spinning [19]	PAN	70–80	7.8 ± 0.3	0.24 ± 0.01	5.5 ± 0.5
	PAN/MWNT (95/5)		10.8 ± 0.4	0.41 ± 0.02	11.4 ± 1.2
	PAN/VGCNF (95/5)		10.6 ± 0.2	0.34 ± 0.01	6.7 ± 0.3
Gel spinning [2]	PAN	~20	22.1 ± 1.2	0.90 ± 0.18	7.4 ± 0.8
	PAN/SWNT (99/1)		28.7 ± 2.7	1.07 ± 0.14	6.8 ± 0.8

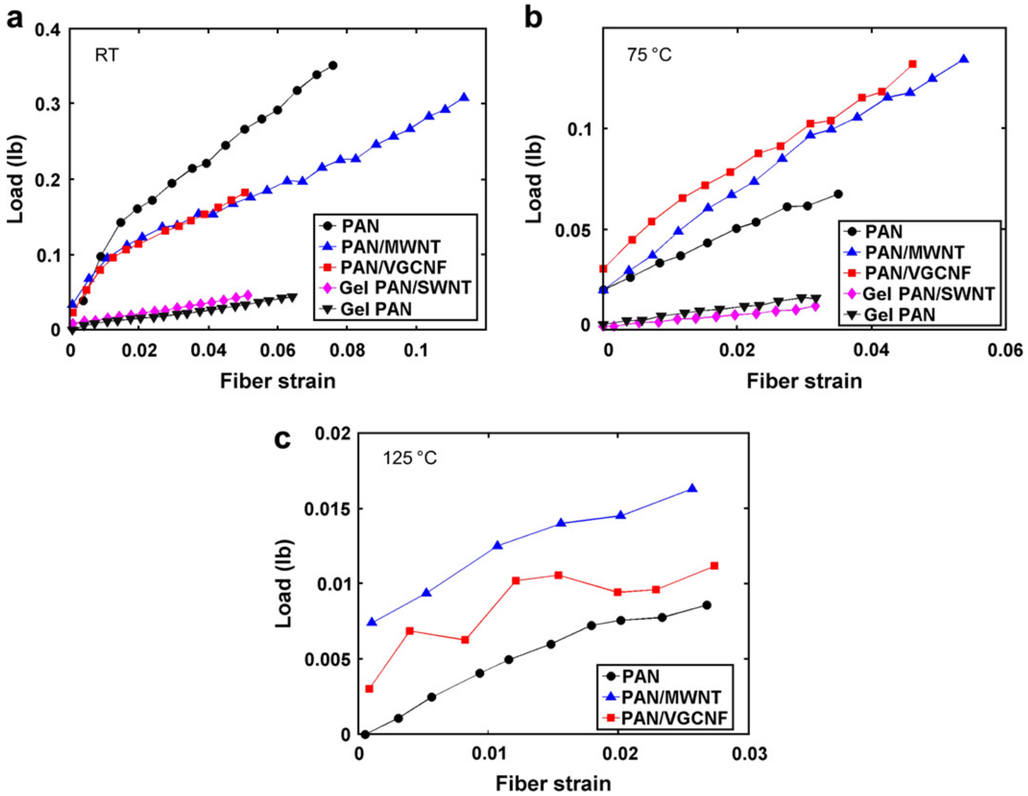

Fig. 1. Tensile load and strain curve for the solution-spun fibers and gel-spun fibers: (a) room temperature; (b) 75 °C and (c) 125 °C.

average over a 20° arc. To obtain 1D azimuthal scans, the intensity was averaged over an annular ring going through the desired reflection such that the intensity at each azimuthal angle is an average over a width of 1 nm^{-1} in q; $q = (4\pi \sin\theta)/\lambda$, λ is X-ray wavelength. A background obtained without sample (e.g., after the fiber broke) was subtracted from each of the scans. The diffraction peaks in the background-subtracted 1D scan were modeled as Gaussian functions described by their positions, widths and heights. To obtain meaningful results, the data were profile fitted with minimum number of variables. To keep the analysis reproducible and simple enough to be automated (nearly 2500 frames were analyzed), the equatorial scans were analyzed by partitioning the scans into two regions, one from $q = 8\ \mathrm{nm}^{-1}$ to 15 nm^{-1} and the other $q = 14.5$–$28\ \mathrm{nm}^{-1}$ (Fig. 3), as implied in a method proposed by Hinrichsen [20]. In each of the segments, a linear baseline was drawn connecting the end points, and two Gaussian peaks were used to fit the data. This scheme provided the most reliable values for the positions of the crystalline peaks, but cannot be used to calculate the crystallinities. This is because the weaker and wider peak in both segments takes into account only a fraction of the contributions of the disordered (non-crystalline or amorphous) domains represented by the baseline; the intense and sharper peaks are due to the crystalline domains. The segmented baseline fit along with the two amorphous peaks in each of the segments approximate well the amorphous profiles used by Chae et al. [19] and the diffuse disorder term, the structure factor of a single chain, calculated by Liu and Ruland [9]. Also, note that the curve fitting of equatorial scan that is used here is consistent with the observation by Joh of a distinct diffuse band due to non-crystalline fraction in PAN [21]. In the PAN/MWNT and PAN/VGCNF samples, an additional Gaussian function was used in the $q = 14$–$25\ \mathrm{nm}^{-1}$ segment to take into account the contribution of d_{002} reflection from the graphitic structure of CNTs.

Meridional data from $q = 21.5$ to $31.5\ \mathrm{nm}^{-1}$ were analyzed. In the case of PAN, the scans were fitted with two Gaussian

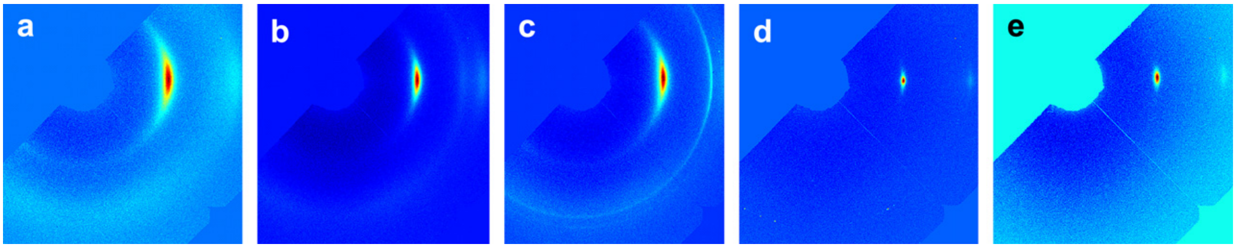

Fig. 2. Examples of the 2D WAXD diffraction patterns of: (a) PAN; (b) PAN/MWNT; (c) PAN/VGCNF; (d) Gel PAN; and (e) Gel PAN/SWNT.

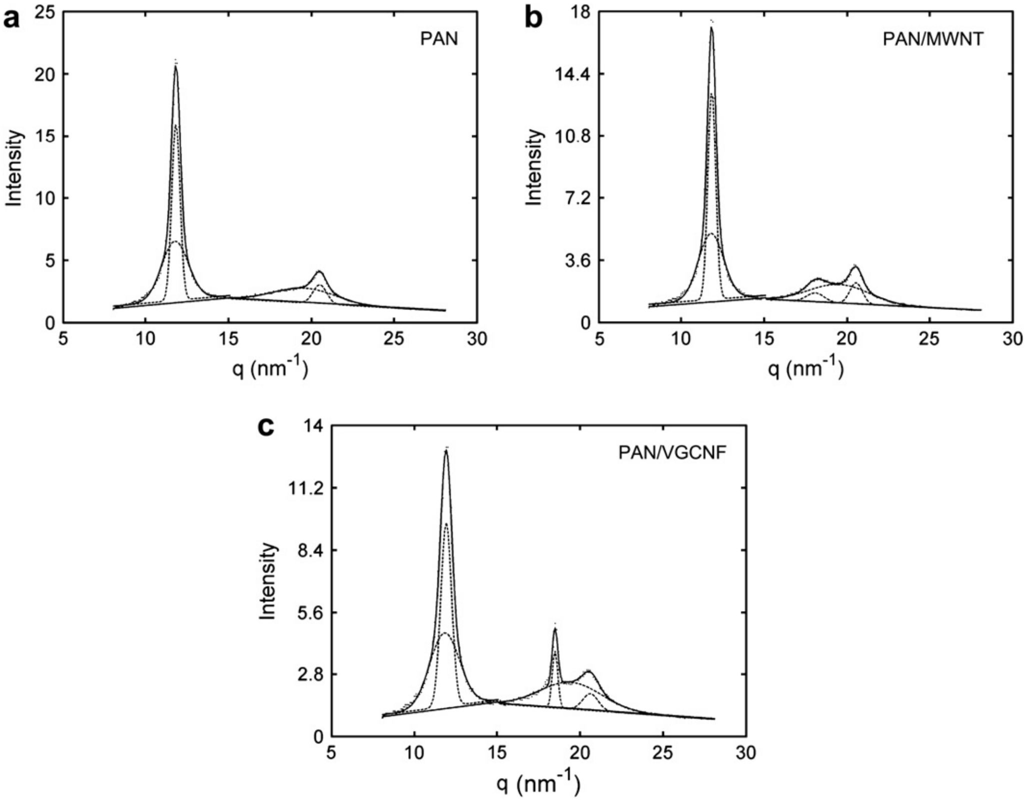

Fig. 3. Profile fitted equatorial scans: (a) PAN; (b) PAN/MWNT; (c) PAN/VGCNF. The data for gel fibers are similar to that of PAN.

functions corresponding to zigzag and helix sequences. The positions of these peaks were used to calculate the chain-axis repeats of the two sequences, and the areas of the peaks were used to calculate the relative fractions of the two sequences. In the case of PAN/MWNT and PAN/VGCNF, additional Gaussian peaks at higher qs were added to take into account the reflections from carbon structures in nanotubes. The carbon peaks were fitted first and subtracted from the intensity profile before fitting the reflections due to zigzag and helix sequences. The center of the mass (CM) of the intensity profile was determined as the weighted sum of the positions of the resolved Gaussian peaks. If x_1 and x_2 are the peak centers, w_1 and w_2 are the respective widths, and A_1 and A_2 are the respective peak heights, then

$$\mathrm{CM} = (x_1 A_1 w_1 + x_2 A_2 w_2)/(A_1 w_1 + A_2 w_2) \qquad (1)$$

The azimuthal scans of the most intense reflection, the first equatorial peaks of PAN and carbon, were analyzed to obtain the degree of orientation of PAN and nanotubes. Orientation was parameterized by the width of the Gaussian peak that was used to fit the scan.

3. Results and discussion

3.1. General

Major features in the WAXD pattern (Figs. 2 and 3) of PAN are the two equatorial reflections corresponding to d-spacings d_1 and d_2 at $q \sim 12.0$ and $20.0\ \mathrm{nm}^{-1}$, respectively [11,17,22], and a diffuse meridional diffraction peaks at $\sim 27\ \mathrm{nm}^{-1}$ [16,23]. In addition to d_1 and d_2 reflections, there is an additional reflection at $q \sim 18\ \mathrm{nm}^{-1}$ in PAN/MWNT and PAN/VGCNF from the separation (d_{002}) of basal planes of graphitic sheets in the nanotubes (Fig. 3b and c). The meridional reflections were diffuse but were of sufficient intensity for detailed analysis (see Section 3.4).

The equatorial diffraction peaks represent lateral order and their d-spacings correspond to the inter-chain spacing. Indexing these reflections is controversial because of the few observed reflections [18,22]; only two intense equatorial peaks were observed in our measurements. Although the splitting of the overlapping peaks has been reported in ultrahigh draw ratio at-PAN [24], the overlapping peaks cannot be meaningfully and reliably resolved in our data. In an orthorhombic unit cell, the first reflection (d_1) is commonly indexed as $110 + 200$, and the second reflection (d_2) as $200 + 310$ [24]. If we assume $d_1 = d_{110} = d_{200}$, $d_2 = d_{310} = d_{020}$, we get $a = 2d_1$, $b = 2d_2$. This is equivalent to assuming a hexagonal unit cell with $a/b = \sqrt{3}$. In a hexagonal unit cell, by indexing d_1 as d_{100} and d_2 as $d_{2\bar{1}0}$, we get $d_1/d_2 = \sqrt{3}$. But in our data we find consistent and reproducible deviation for the d_1 to d_2 ratio from $\sqrt{3}$ that cannot be attributed to experimental error, especially during elongation (Fig. 4). Therefore, orthorhombic cell is a more appropriate description of our data and both d_1 and d_2 spacings are the average of the two overlapping peaks. Thus, although, our data suggest that unit cell is not hexagonal, the overlapping reflections do not permit

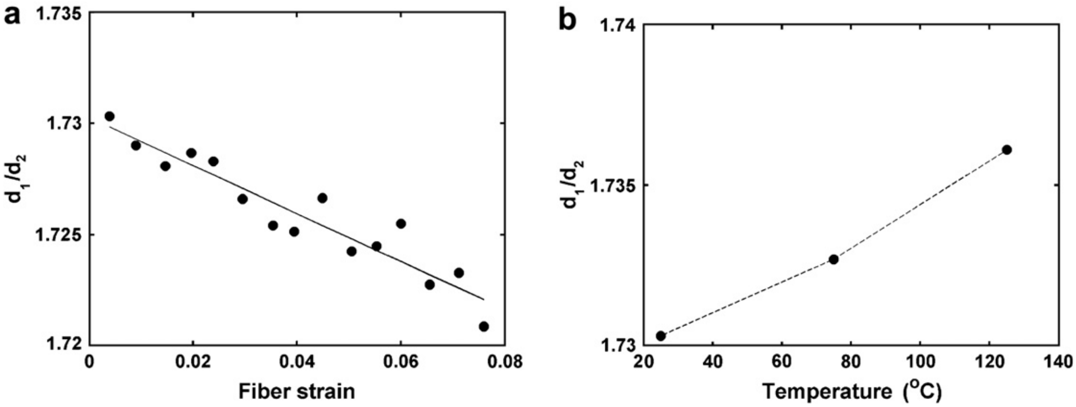

Fig. 4. d_1/d_2 Ratio as function of (a) strain from data from PAN fibers at RT and (b) temperature.

us to obtain orthorhombic unit cells. Therefore, in this paper we present d_1 and d_2 values rather than calculate the unit cell dimension.

The changes of the structures of nanotubes were examined by monitoring the d_{002} spacing of the graphitic planes (d_{Graphite}). X-ray powder measurements of MWNT show the main carbon peak to be at 0.342 nm, which is same as the d_{002} interlayer spacing of graphite sheets [19]. Our measurements are in good agreement with these data. The interplanar spacing of graphitic layers increase with temperature (Fig. 5a), and decrease in response to axial fiber strain most noticeably in PAN/MWNT (Fig. 5b). The deviation from linearity in Fig. 5a could be related to the constraints imposed by the PAN matrix. Although we have only three points, we speculate that the interaction between the PAN matrix and carbon nanotubes/nano-fibers could influence the thermal expansion coefficient (α) of carbon reinforcements. The reported α values along the radial direction in MWNT range from $1.6 \times 10^{-5}\ \mathrm{K}^{-1}$ to $2.6 \times 10^{-5}\ \mathrm{K}^{-1}$, and is about the same as that along the c-axis of a graphite crystal ($2.5 \times 10^{-5}\ \mathrm{K}^{-1}$) [25]. If there is a strong interaction between PAN matrix and MWNT, then the large mismatch in α between PAN matrix and MWNT could increase the α of carbon reinforcement to ensure continuity across the MWNT/PAN boundary. Thus,

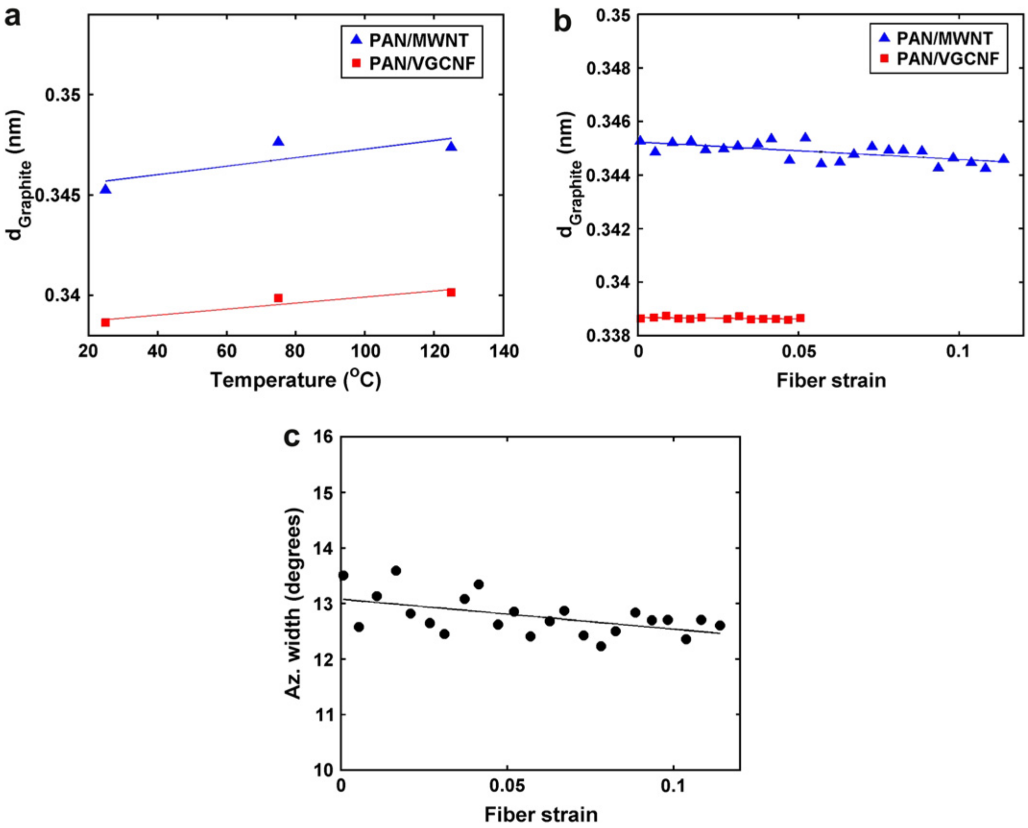

Fig. 5. (a) Effect of temperature on d-spacings of carbon in unstressed fibers derived from the Bragg's peak for nanotubes; (b) changes in the d-spacing of carbon as a function of strain derived from the Bragg's peak of nanotubes at room temperature; (c) degree of orientation of MWNT in the form of the azimuthal breadth.

α is large between room temperature to 75 °C. Between 75 and 125 °C, as the carbon/PAN interaction decreases at higher temperatures, the α decreases to that of graphite or isolated single MWNT. Note that the interaction is weaker between VGCNF and the PAN matrix than between MWNT and PAN [19]. Therefore, the overall thermal expansion in PAN/VGCNF is less than in PAN/MWNT.

The strain-induced changes in CNTs, even though they are an order of magnitude smaller than corresponding changes in the PAN matrix, indicate that the load is being transferred to the CNT (MWNT) reinforcements. If the MWNT is approximated by graphite layers, the relatively small reduction of separation of basal planes of MWNT upon axial stretching can be ascribed to the low Poisson ratio (0.07) of *c*-axis lattice contraction in graphite [26]. This is supported by the increase in the orientation of the MWNT with strain as indicated by the small decrease in the azimuthal width of its equatorial reflection during elongation at room temperature (Fig. 5c). Similar trend was seen with PAN/VGCNF fibers but could not be reliably calculated because in these fibers the graphite peaks split along the azimuth due to a 15° tilt of the graphite plane with respect to the fiber axis.

3.2. Orientation

Orientation of the PAN crystallites was monitored using the azimuthal width w of equatorial d_1 peak, and that of the nanotubes from the azimuthal width of the graphitic (002) reflection. w was calculated from the equation

$$I = I_0 \exp\left[-\left(\frac{x - x_0}{w}\right)^2\right] \tag{2}$$

where I is the intensity at an azimuthal position denoted by x, x_0 is the peak position where the intensity is I_0. w is related to the commonly used full-width at half-maximum by: FWHM $= 2\sqrt{\ln 2}w$. The data were fitted to one Gaussian function except for the carbon peak in VGCNF wherein two Gaussian peaks of equal width were used to account for the tilt of the graphitic sheets away from the fiber axis [6]. The orientation data for all the fibers at room temperature are plotted in Fig. 6 as a function of the fiber strain. The much higher orientation in the gel-spun fibers, as indicated by the smaller azimuthal width of the reflections, is obvious because these fibers were subjected to higher draw ratios than the conventional solution-spun fibers. The higher orientation of PAN in nanocomposite fibers shows that the nanotubes facilitate the PAN orientation at room temperature. Fig. 6 also shows the expected increase in the degree of orientation, plotted as the azimuthal width, which is inversely related to the degree of orientation, with strain. Analyses of all the data of the type shown in Fig. 6 are summarized in Table 2 in the form of initial value of the azimuthal width and the slope of the curve in Fig. 6. These two correspond to the initial orientation and the increase in orientation during elongation. Interestingly, the

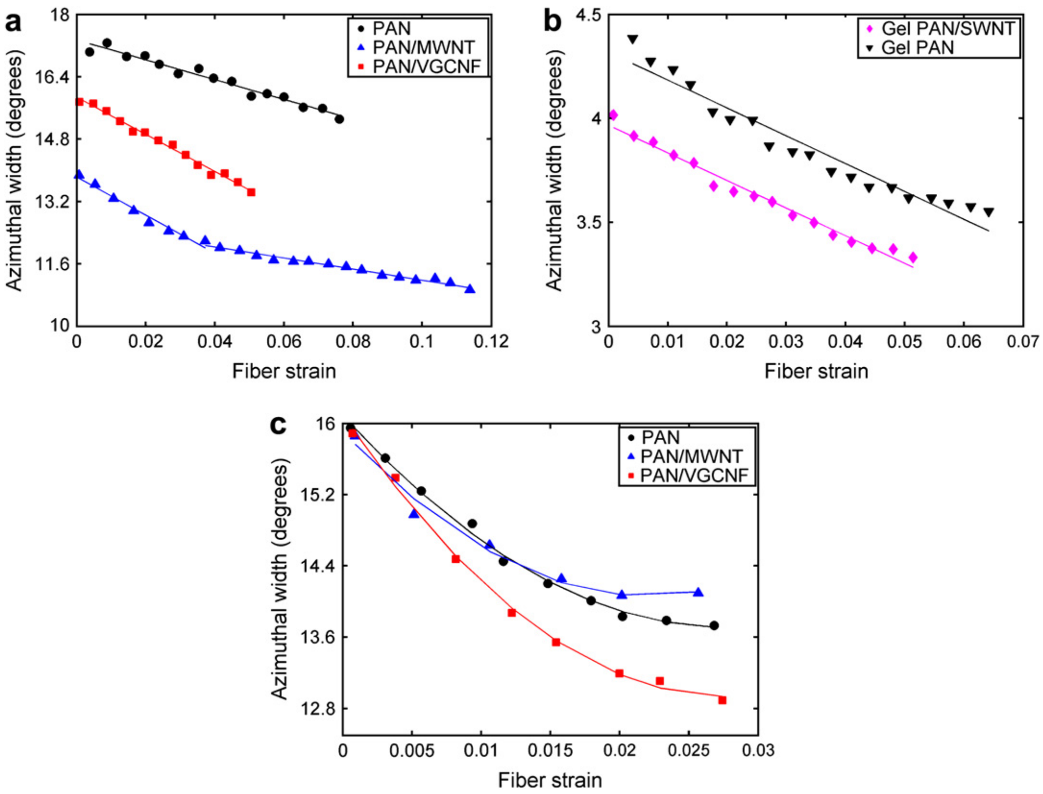

Fig. 6. (a) Degree of orientation of PAN in the form of the azimuthal breadth of its first equatorial peak plotted as a function of strain for solution-spun PAN and nanocomposites at room temperature; (b) degree of orientation for gel-spun fibers at room temperature; (c) degree of orientation for solution-spun fiber at 125 °C.

Table 2
Slope of azimuthal width of the d_1 reflection vs. fiber strain

	Room temperature		75 °C		125 °C	
	Initial value[a]	Slope[b]	Initial value[a]	Slope[b]	Initial value[a]	Slope[b]
Control PAN	17.4 ± 0.1	−28.9 ± 3.5	15.3 ± 0.3	−54.1 ± 8.1	15.9 ± 0.0	−102.5 ± 9.2
PAN/MWNT	14.1 ± 0.6	−46.6 ± 3.9	14.3 ± 0.4	−68.7 ± 3.1	15.6 ± 0.2	−84.0 ± 5.8
PAN/VGCNF	15.3 ± 0.9	−45.0 ± 6.9	14.9 ± 1.1	−41.0 ± 4.8	15.8	−130.32
Gel PAN[b]	3.9 ± 0.1	−6.3 ± 0.9	4.6 ± 0.1	−23.0 ± 0.8		
Gel PAN/SWNT[b]	4.7 ± 0.6	−16.3 ± 5.7	4.7 ± 0.6	−9.8 ± 0.6		

[a] At the start of the elongation, the azimuthal width decreased rapidly in Gel PAN at room temperature and Gel PAN/SWNT at 75 °C. The initial values given are the extrapolated values after excluding those few initial points that have a large spread.

[b] The slopes are measured from linear portion of the stress-strain curve at low strains. In most of cases, the slope levels off at high strain (Fig. 6).

rate of this increase in orientation with strain depends on the fiber. This value, in units of azimuthal degrees per unit macroscopic strain calculated from a linear fit to the data, is much higher in the presence of nanotubes than that without nanotubes; at room temperature the values are: 46.6 for PAN/MWNT (which drops to 15.4 at high strains) and 45.0 PAN/VGCNF compared to 28.9 for PAN. The gel-spun fibers are highly oriented to begin with, and the values for gel PAN and gel PAN/SWNT are 6.3 and 16.3, respectively. Thus, it appears that nanotubes facilitate the orientation of PAN crystals in solution- and gel-spun fibers even at room temperature.

Table 2 shows that the degree of orientation of PAN increases with strain even at 125 °C, above the glass transition temperature (see Fig. 6c). This is interesting because there was no appreciable change in other structural parameters (lateral spacing d_1, zigzag fraction and the axial repeat; see Sections 3.3 and 3.4) at 125 °C. This suggests that although the PAN crystals were unable to respond to external loads and the amorphous (non-crystalline) matrix carried most of the load, the PAN crystallites could reorient during elongation. It is possible that at these temperatures ($>T_g$) fluid like amorphous matrix facilitates the rotation of the crystallites. The changes in orientation as well as in other aspects of the structure (e.g., lateral spacing (d_1), zigzag fraction and the axial repeat; see Sections 3.3 and 3.4) in response to the fiber strain at 75 °C were similar to that at room temperature.

3.3. Equatorial scattering and lateral order

These equatorial d-spacings are related to the inter-molecular distance of the PAN chains, and are affected by factors such as draw ratio, solvent residues, as well as temperature. The data from the unstrained fiber at three different temperatures are summarized in Table 3. These data show that in the presence of a small amount of CNT, PAN crystals have denser structure (smaller d_1), consistent with the previously published results [2]. The d_1-spacing in PAN/MWNT and PAN/VGCNF is approximately between that of PAN and gel-spun fibers. Re-examination of the data presented in a previous paper [19] in fact showed a similar behavior (0.5283 in control PAN vs. 0.5271 nm in PAN/MWNT and PAN/VGCNF). The solution-spun PAN control fiber had the largest d_1-spacing and gel-spun PAN and PAN/SWNT had the smallest value even at elevated temperatures (e.g., 75 °C). In the fibers that were studied, the range of d-spacing was larger for the first equatorial peak (d_1) than for the second peak (d_2). As a result, the d_1/d_2 ratio, which is sometimes used as a proxy for the shape of the unit cell, decreased during elongation from ∼1.73 to1.72 in solution-spun fibers and from ∼1.72 to 1.71 in gel-spun fibers; this ratio is 1.732 for a hexagonal lattice.

Table 3
d-Spacings (in nm) in unstressed state

Temperature (°C)	Control PAN	PAN/MWNT	PAN/VGCNF	Gel PAN	Gel PAN/SWNT
25	0.5270	0.5246	0.5246	0.5244	0.5217
75	0.5312	0.5308	0.5284	0.5273	0.5293
125	0.5396	0.5380	0.5384		

Table 3 also shows the thermal expansion of d_1-spacing of the PAN matrix in the unstrained state for the various types of samples in this study. The increase in the d-spacing with temperature is about the same above and below T_g in PAN/MWNT and is twice larger above T_g than below T_g in control PAN and PAN/VGCNF.

The value of d_1 and d_2 are known to decrease with increasing draw ratio [2]. These decreases in d-spacings with fiber elongation correspond to a contraction of the transverse dimensions of the PAN unit cell. For the purposes of comparison between the fibers, the changes in the d-spacings with fiber strain were monitored by following the slope of the plot in the ε_{lat} vs. fiber strain (up to 3%) (Fig. 7), rather than the absolute value of the d-spacing. The ε_{lat} is the lateral strain of PAN defined as

$$\varepsilon_{lat} = -\left(d_1' - d_1\right)/d_1 \quad (3)$$

where d_1 and d_1' are unstressed and stressed d_1-spacing, respectively [22].

Fig. 7 along with Table 3 shows an almost linear decrease in d_1 and d_2 with fiber strain at low elongations at both room temperature and 75 °C; the curves tend to plateau out at higher elongations especially at 75 °C. Absence of any appreciable changes in the peak positions and intensity with strain at 125 °C (data not shown) indicate that the crystal structure is the least affected by external load at this temperature. It is worth noting that at high temperature such as 75 °C, the d-spacing appears to stop decreasing, and even increase in PAN/MWNT, before the eventual failure (Fig. 7c and d). Note also that the orientation ceases to improve beyond certain

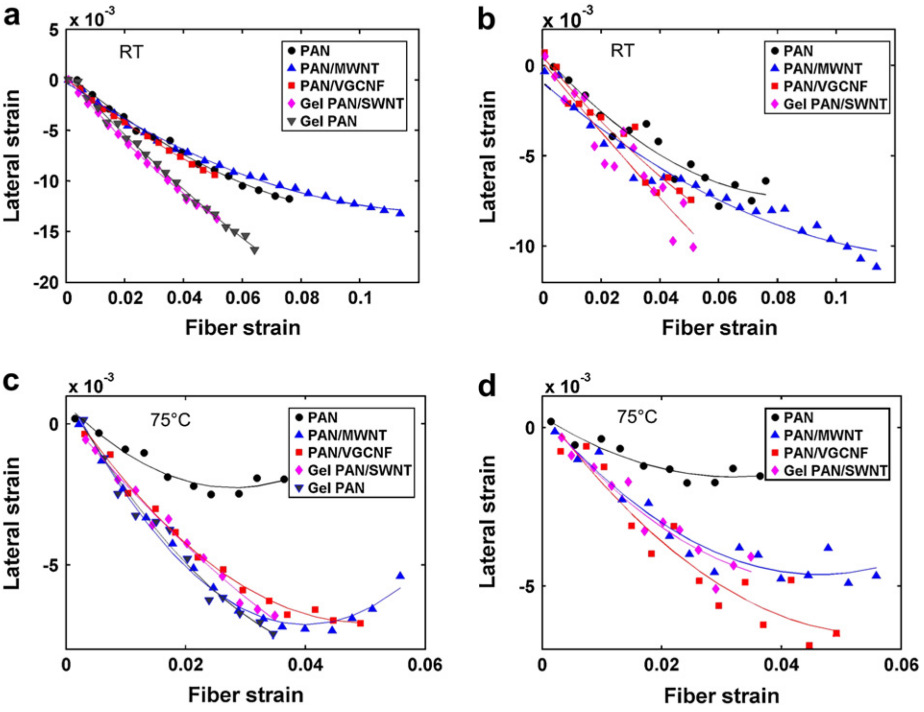

Fig. 7. (a) Plot of the lateral crystal strain based on d_1 vs. axial fiber strain of PAN at room temperature; (b) slopes of the curve of lateral strain based on d_2 vs. fiber strain at room temperature; (c) and (d) are the same as (a) and (b) except at 75 °C.

strain (Fig. 6; 75 °C data not shown). These results suggest that the linkages to the crystalline regions fail first causing the unit cell to relax while the amorphous regions continue to bear the load up until the eventual failure.

It can be seen that the slope of lateral X-ray strain vs. macroscopic fiber strain curve for the gel-spun fibers differs greatly from those of the solution-spun fibers. In particular, note that while the slope decreases at high strains for the solution-spun fibers, it remains nearly constant at all strains for the gel fibers till failure. Since lateral strain is an indirect measure of the axial stress, this suggests that while the fraction of the load transferred to the PAN crystals decreases at high strains in solution-spun fibers, this fraction remains essentially unchanged in the gel fiber. This is indicative of the stronger linkages between the crystal and the amorphous domains in the gel-spun fibers. This could account for the observation that, unlike in conventional and solution-spun-fiber, the linear stress–strain curve in gel-spun fibers is almost linear (Fig. 1) [2].

The slopes of the plots in Fig. 7 are the measures of the load shared by the PAN crystals in these fibers, assuming that the PAN modulus in the composite fiber is the same as in the control PAN. The absolute values of the slopes calculated from the initial straight line portion of the curves, i.e., at low strains, are shown in Fig. 8. The data for the gel fibers at 125 °C could not be obtained, as it was difficult to maintain the precise temperature on this thin filament without overheating it. At room temperature, the slopes in both gel PAN and the gel PAN/SWNT composite, are nearly 30–40% larger than solution-spun fibers. At 75 °C, this slope drops to about 50% in PAN but remains essentially unchanged in PAN/MWNT, PAN/VGCNF and gel PAN indicating that the PAN crystals in these fibers continue to share the load unlike in the solution-spun PAN fiber. Although the slope decreased in gel PAN/SWNT, it was still twice as much as solution-spun PAN. Analysis of the PAN reflections at 125 °C, which were still quite intense for detailed analysis, showed that the equatorial d-spacings decreased with strain at lower temperatures. However, the slopes of the lateral strain vs. fiber strain plot in all the fibers were an order of magnitude smaller than at room temperature. This indicates that the PAN crystallites in PAN and its composite carry almost no load above glass transition temperature of PAN.

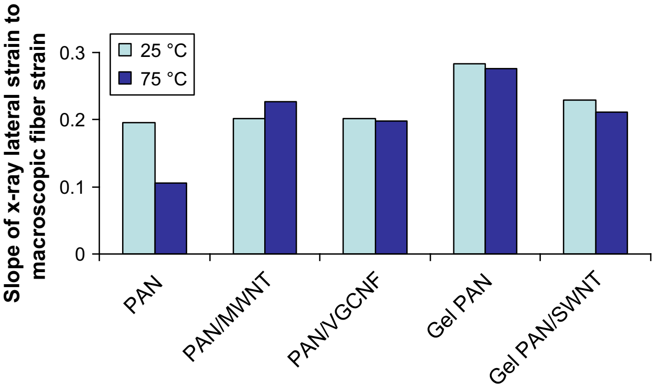

Fig. 8. The slope of X-ray lateral strain based on d_1 to macroscopic fiber strain.

3.4. Meridional scattering and axial structure

A diffuse peak at $q \sim 27\ \text{nm}^{-1}$ was observed in the meridional scans of PAN. These are overlapping peaks due to different periodicities along the chain axis (Fig. 9a and b). The scans obtained at various temperatures indicate that the temperature has little effect on the axial periodicity (data not shown). In addition to the periodicities due to the zigzag and helical conformation of PAN, we also see the d_{101} reflection of carbon in the PAN/MWNT and PAN/VGCNF fibers (Fig. 9c). The meridional data from gel-spun PAN fibers were too weak to be analyzed. The shape and the position of these peaks were analyzed as a function of fiber strain at various temperatures to determine the changes in the dimensions along the chain-axis. We found that the position of the graphite peak in the meridional scans shifts to lower angles, consistent with the decrease in the lateral spacing (Fig. 5b), indicating that load is being shared by the nanotubes inclusions. These shifts were quite small (2% in ~2.1 nm) but could be measured in PAN/MWNT and not reliably in PAN/VGCNF. The longitudinal strain of the PAN chains was estimated from the shift in the average position of the peaks shown in Fig. 9a and b. The CM of the intensity profile, centroid to be more precise, can be used as a measure of axial periodicity [22,23]. It has been previously reported that the CM shifts to lower q with increase in stress at room temperature [22].

There could be different mechanisms that account for the changes in the axial spacing with strain as determined by the CM. One is the stretching of the zigzag and the helix sequence. The other is the increase in the fraction of zigzag sequence at the expense of the helical fraction; the chain-axis repeat is 0.25 nm for the zigzag chains, and 0.23 nm for the helical chains [9,22–24]. To monitor the changes in the fraction of intensity due to the zigzag sequence, and the changes in the d-spacing of helix and zigzag sequences in response to the strain, the broad meridional peak was resolved into two peaks at $q \sim 25\ \mathrm{nm}^{-1}$ and $q \sim 27\ \mathrm{nm}^{-1}$, corresponding to planar zigzag chain and 3_1 helix conformations, respectively [2,16,22–24]. To keep the number of variables to a minimum, the two Gaussian peaks were assigned the same width, which is equivalent to assuming that the crystallite sizes of the two sequences are about the same. Three quantities were calculated to capture these changes along the chain-axis: the centroid (Fig. 10a and c), axial repeat of helix and zigzag, and the fraction of the zigzag sequence (Fig. 10b and d).

This conclusion that helix-rich chains in the unstressed polymer transform into zigzag rich structures upon stretching is consistent with the changes in the equatorial scan. From the unit cell dimensions isotactic PAN, in which PAN is known to be helical, the crosssectional area of a helical PAN can be calculated to be 0.324 nm^2 [23]. Similarly, from the unit cell dimensions of syndiotactic PAN, which is known to have zigzag chains, the crosssectional area of a zigzag PAN can be calculated to be 0.306–0.312 nm^2 [15]. Our value of cross sectional area decreases from 0.32 to 0.31 nm^2 upon stretching. In fact

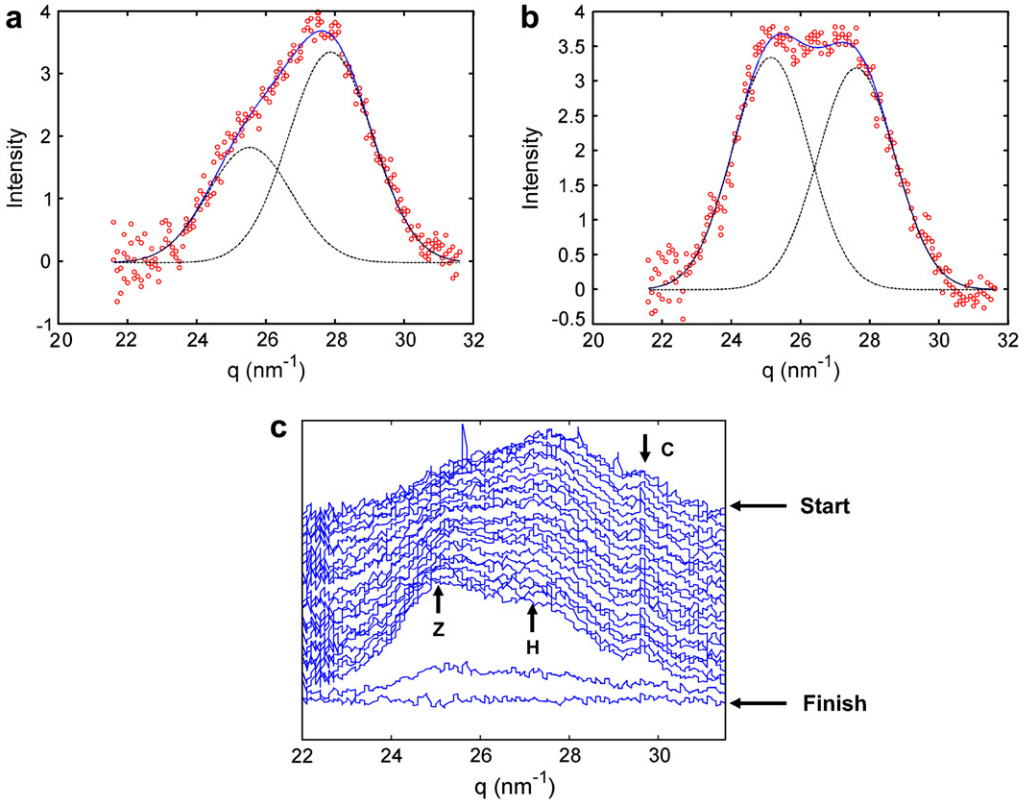

Fig. 9. Profile fitted meridional scans of the PAN fiber at room temperature: (a) unstrained fiber; (b) just prior to failure. Open circles are experimental data, dashed lines are two Gaussian functions of equal width, and continuous line through the observed data is the sum of these two Gaussian functions; (c) an example of overlay of the meridional scans from starting to failure; the one shown is from PAN/MWNT at room temperature. The letters Z, H and C point to the diffraction peaks from zigzag – PAN, helix – PAN and d_{101} – carbon, respectively.

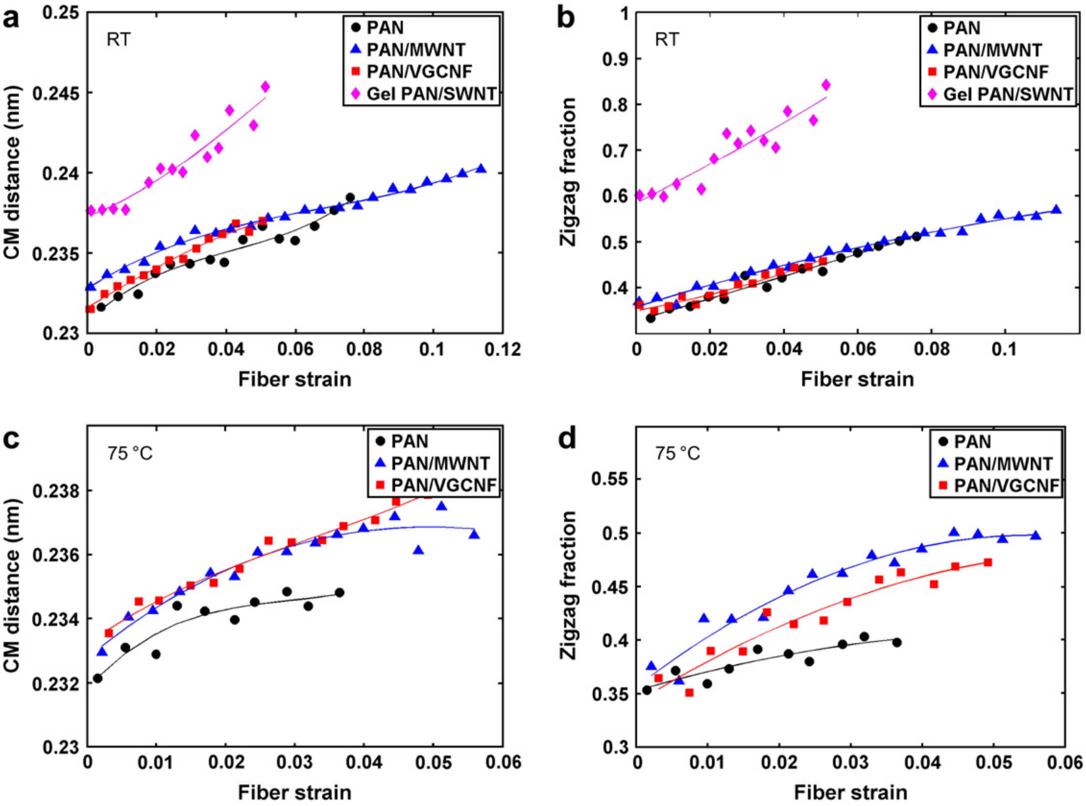

Fig. 10. (a) Plot of the CM vs. axial fiber strain of PAN at room temperature; (b) plot of zigzag sequence fraction vs. fiber strain at room temperature; (c) and (d) are the same as (a) and (b) except at 75 °C.

we find a nice correlation between the cross sectional area and the zigzag fraction as shown in Fig. 11.

The increase in the fraction of the intensity due to zigzag sequence relative to the total diffraction intensity under the meridional peak (Fig. 10b) shows that as the fiber is stretched, the zigzag peak becomes stronger and the helix peak becomes weaker. Thus, the shift in the CM with strain is largely due to a shift in the population of chains from helix to zigzag conformation in response to macroscopic deformation. Both the lateral spacing and the axial spacing appear to be linearly correlated with the fraction of zigzag sequence (see Fig. 12; Section 3.5). Transformation from helix to zigzag conformation and a decrease in lateral dimension of the unit cell can be taken as a measure of the load transfer to the crystalline domains.

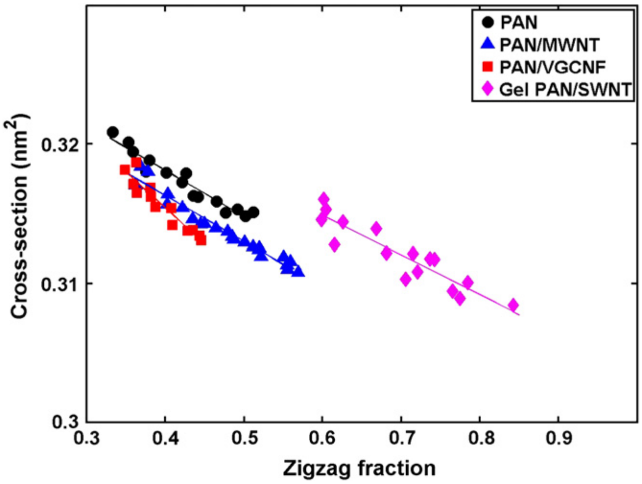

Fig. 11. Correlation between cross-sectional area and the zigzag fraction in four PAN fibers from the data obtained at RT.

In gel-spun PAN/SWNT fibers the meridional peak (the peak was weak in gel PAN for analysis) occurs at a lower *q* (larger CM) and the zigzag fraction is greater than in solution-spun fibers. This could be due to the presence of CNT in addition to being processed by gel spinning (Fig. 10). More importantly, the larger rate of change in the chain-axis repeat and the zigzag fraction with fiber strain in the gel-spun fibers suggests that gel spinning greatly increases the fraction of load carried by PAN crystallites. Recall that we came to the same conclusion in Section 3.3. Therefore, there appears to be a more efficient load transfer to the crystalline domains, resulting in better mechanical properties in gel-spun composite fibers. MWNT appears to bring about similar but much smaller change in the axial structure of PAN, favoring zigzag sequence as indicated by the small shift in the centroid to lower *q* compared to PAN and by the smaller equatorial spacing (Table 3).

3.5. Reversibility

We examined the extent of reversibility of the structural changes with fiber strain, especially the correlation between the fraction of zigzag sequence and the lateral order in PAN

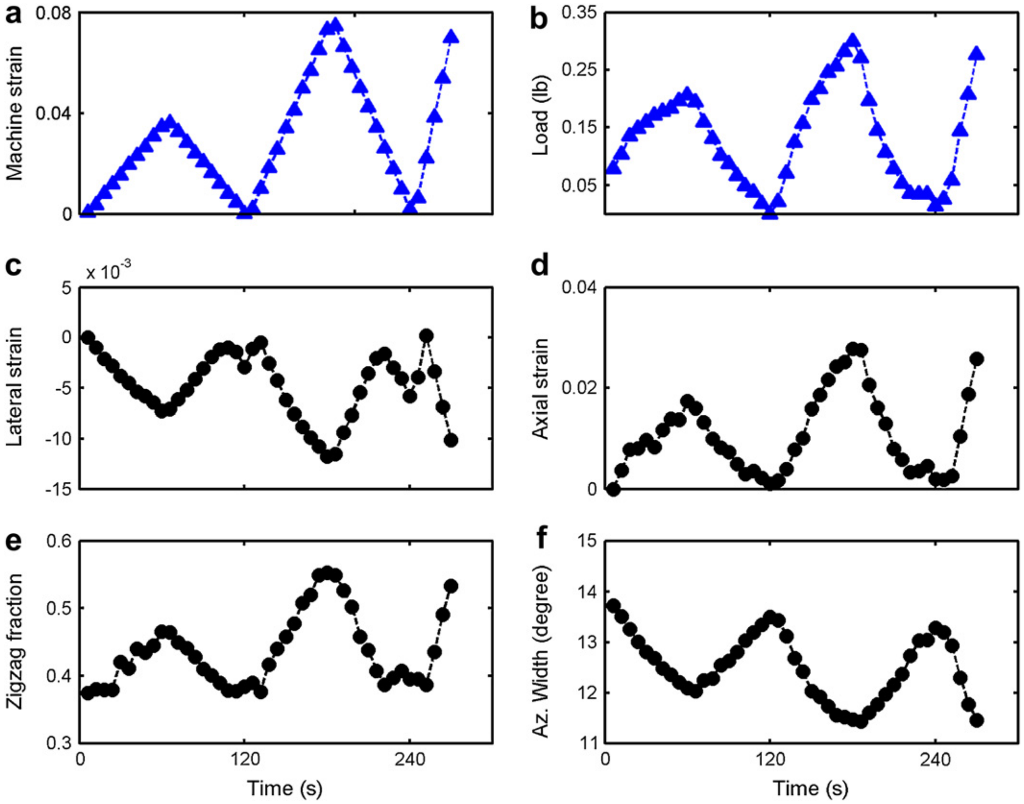

Fig. 12. Reversibility of structural changes in PAN/MWNT. Blue triangles are the machine strain deducted from the displacement of the grips holding the samples. Black circles are the parameters derived from X-ray scans (except load). Both are illustrated as functions of time: (a) machine strain; (b) tensile load; (c) lateral strain of crystalline PAN derived from d_1; (d) Axial strain derived from CM; (e) fraction of zigzag sequence and (f) azimuthal widths (for interpretation of the references to colour in this figure legend, the reader is referred to the web version of this article).

in the neat polymer and the nanocomposites. Experiments were carried out in quasi-static mode. In the first cycle, the load was increased to a value far below the failure strain so as to stay within the elastic limit, and then reduced to zero at the same rate. Based on the data in Fig. 1, the fiber (machine) strain for the first cycle during the reversibility test was therefore chosen to be <2% for PAN and <4% for PAN/MWNT. In the second cycle the fiber was strained to a value above the expected elastic limit and then relaxed. In the third cycle, the fiber was stretched to failure. The strain rates for the first, second and the third cycles were 0.02, 0.04 and 0.1, respectively, for PAN, and 0.04, 0.08 and 0.16, respectively, for PAN/MWNT. The data are plotted as a function of time in Fig. 12. PAN/MWNT fiber, in the form of lateral strain determined from lateral spacing (d_1), axial strain determined from meridional CM spacing (and defined in the same manner as lateral strain: $\varepsilon_{\mathrm{axial}} = -(d'_{\mathrm{CM}} - d_{\mathrm{CM}})/d_{\mathrm{CM}}$; where d'_{CM} is d-spacing during elongation and d_{CM} is the initial value of axial d-spacing), the chain conformation as indicated by the zigzag fraction and the orientation of PAN crystals. Similar changes were in control PAN.

There appears to be two distinct regimes in the stress-strain curves especially at room temperature (Fig. 1a): higher modulus regime at low strains (<2%) and lower modulus regime at higher strains. The changes in the axial repeats of the zigzag and helix sequences (Fig. 13) show that both the zigzag and the helical chains in PAN underwent a longitudinal extension during initial elongation; thereafter, there is a slower increase in their repeat-distance while the zigzag fraction increases (Fig. 12e). There appears to be two mechanisms that contribute to the fiber stiffness: one dominated by extension of the chains at low strain (<1.5%) that gives rise to higher modulus and the other by the changes in the conformation from helix to zigzag at higher strains that gives rise to lower modulus [23]. The behavior is somewhat different in PAN/MWNT, which could in part explain the lower strain to failure in PAN than in PAN/MWNT (Fig. 1).

Two regimes in the stress–strain curves have also been reported by Sawai et al. for isotactic PAN. They also found three regimes in the stress–strain curves of atactic PAN [23]. In addition to the explanation that we offered in the previous paragraph for the existence of the high modulus first regime followed the low modulus second regime, they suggest that in atactic PAN, the helical fraction completely disappears, and the planar zigzag conformation that is present at high strain causes the modulus to increase rapidly in the third regime. They further suggest that in isotactic PAN, the helical fraction persists till failure, and the transformation to zigzag continues till failure. We also find that conformational changes in our fibers continue up to the point of failure, and the zigzag fractions increased from ~30% to ~50% as the fibers were elongated to failure. One significant observation in Fig. 12 is

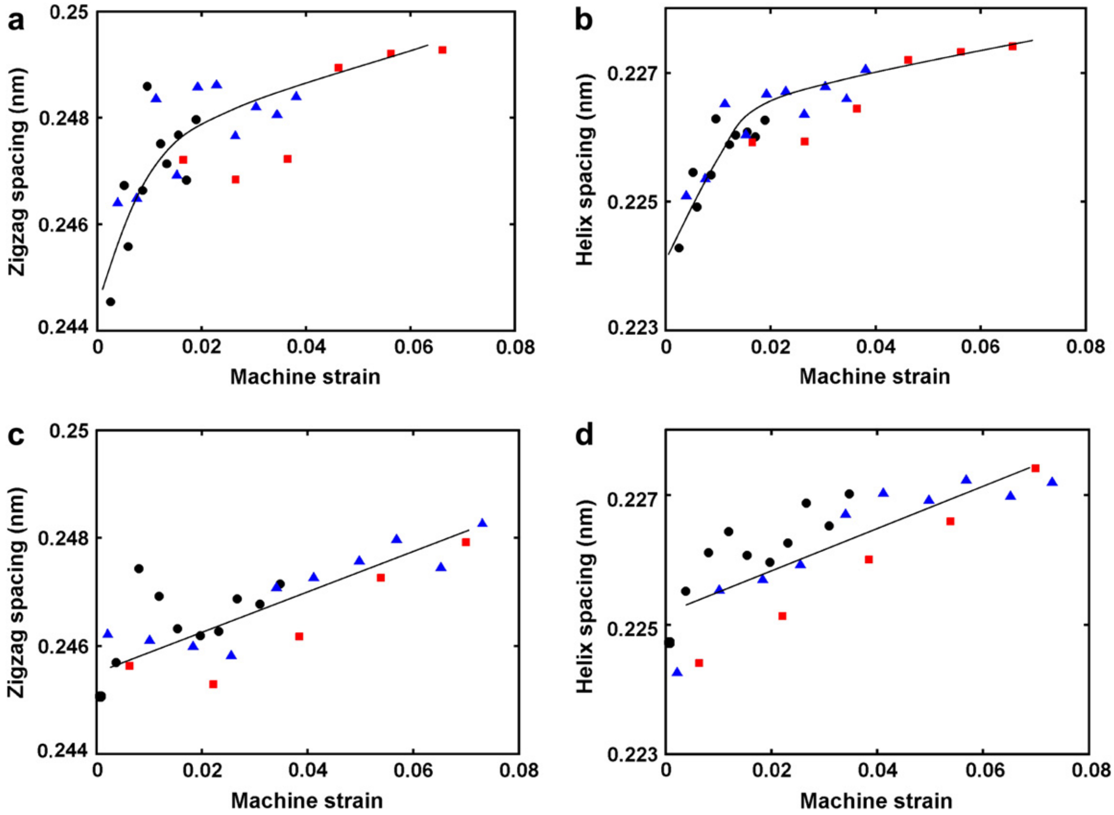

Fig. 13. Zigzag spacing and helix spacing as function of machine strain in successive loading–unloading cycles. Black circles denote the first cycle. Blue triangles denote the second cycle. Red squares denote the third cycle. (a) Increase of zigzag spacing in loading cycles; (b) increase of helix spacing in loading cycles; (c) and (d) are the same as (a) and (b) except for PAN/MWNT (for interpretation of the references to colour in this figure legend, the reader is referred to the web version of this article).

that many of the structural changes including the helix–zigzag conformational changes appear to be, for the most part, completely reversible even when elongated beyond the elastic limit. This is also confirmed by the plots of the changes in the helix and zigzag chain-axis repeats (Fig. 13).

4. Conclusions

1. The lateral dimensions of PAN unit cell decrease as the axial fiber strain is increased at temperature below T_g. The magnitude of the decrease in lateral crystal dimensions with fiber strain suggests that both CNT inclusion and gel spinning can bring about more efficient load transfer at 75 °C.
2. Evidence for the load shared by the CNT comes in the form of contraction of the lateral spacing of the graphitic sheets, which was small compared with that of PAN matrix, increased orientation of the CNT, and marginal extension graphitic sheets along the fiber axis.
3. The CM (centroid) of the meridional intensity profile is used as a measure of the effective axial repeat of PAN chains. Axial extension of zigzag and helix chains as well as the conversion from helix to zigzag conformations contribute to this shift in CM. The relative magnitude of the two contributions depends on the strain and the presence of CNT. As in the lateral structural change, the addition of CNT and gel spinning affects the axial PAN crystal structure, leading to the highly oriented zigzag structure.
4. The orientation of PAN increases with the increase of axial fiber strain, even at 125 °C even though the unit-cell dimensions of PAN ceases to change at 125 °C. At room temperature, the existence of nanotubes was conducive to higher degree orientation of PAN chains.
5. Load transfer to PAN crystalline domains in CNT-containing fibers was better than in control PAN near T_g.
6. The conformational changes that occur during elongation are for the most part reversible.
7. The above observation suggests that CNTs, while enhancing the properties of the composite as reinforcing elements, also augment the contribution of the PAN matrix.

Acknowledgments

We wish to thank S. Weigand, Mike Gus for making it possible to do this work at the Argonne Photon Source (APS). This work was funded by NSF grant DMR-0513926. Portions of this work were performed at the DuPont-Northwestern-Dow Collaborative Access Team (DND-CAT) Synchrotron Research Center located at Sector 5 of the Advanced Photon Source. DND-CAT is supported by the E.I. DuPont de Nemours & Co., the Dow Chemical Company, the U.S. National Science Foundation through Grant DMR-9304725 and the

State of Illinois through the Department of Commerce and the Board of Higher Education Grant IBHE HECA NWU 96. Use of the Advanced Photon Source was supported by the U.S. Department of Energy, Office of Science, Office of Basic Energy Sciences, under Contract No. W-31-109-ENG-38. Fiber studies at Georgia Tech are supported by a grant from the Air Force Office of Scientific Research (FA 9550-07-1-0233).

References

[1] Guo H, Sreekumar TV, Liu T, Minus M, Kumar S. Polymer 2005;46:3001–5.
[2] Chae HG, Minus ML, Kumar S. Polymer 2006;47:3494–504.
[3] Chae HG, Minus ML, Rasheed A, Kumar S. Polymer 2007;48:3781–9.
[4] Koganemaru A, Bin Y, Agari Y, Matsuo M. Adv Funct Mater 2004;14(9):842–50.
[5] Sreekumar TV, Liu T, Min BG, Guo H, Kumar S, Hauge RH, et al. Adv Mater 2004;16(1):58–61.
[6] Uchida T, Anderson DP, Minus M, Kumar S. J Mater Sci 2006; 41(18):5851–6.
[7] Ye H, Lam H, Titchenal N, Gogotsi Y, Ko F. Appl Phys Lett 2004; 85(10):1775–9.
[8] Bohn CR, Schaefgen JR, Statton WO. J Polym Sci 1961;55:531–49.
[9] Liu XD, Ruland W. Macromolecules 1993;26:3030–6.
[10] Bashir Z, Tipping AR, Church SP. Polym Int 1994;33:9–17.
[11] Colvin BG, Storr P. Eur Polym J 1974;10:337–40.
[12] Svegliado G, Talamini G, Vidotto G. J Polym Sci Part A Polym Chem 1967;5:2875–81.
[13] Hu XP. J Appl Polym Sci 1996;62:1925–32.
[14] Hobson RJ, Windle AH. Macromolecules 1993;26:6903–7.
[15] Hobson RJ, Windle AH. Polymer 1993;34(17):3582–96.
[16] Sawai D, Yamane A, Takahashi H, Kanamoto T, Ito M, Porter RS. J Polym Sci Part B Polym Phys 1998;36:629–40.
[17] Allen RA, Ward IM, Bashir Z. Polymer 1994;35(10):2063–71.
[18] Bashir Z. J Polym Sci Part B Polym Phys 1994;32:1115–28.
[19] Chae HG, Sreekumar TV, Uchida T, Kumar S. Polymer 2005;46: 10925–35.
[20] Hinrichsen G. J Polym Sci Polym Symp Series C 1972;38:303–14.
[21] Joh Y. J Poly Sci Polym Chem Ed 1979;17:4051–67.
[22] Allen RA, Ward IM, Bashir Z. Polymer 1994;35(19):4035–40.
[23] Sawai D, Yamane A, Kameda T, Kanamoto T. Macromolecules 1999;32:5622–30.
[24] Yamane A, Sawai D, Kameda T, Kanamoto T, Ito M, Porter RS. Macromolecules 1997;30:4170–8.
[25] Wong M, Paramsothy M, Xu XJ, Ren Y, Li S, Liao K. Polymer 2003;44:7757–64.
[26] Kelly BT, Martin WH, Nettley PT. Phil Trans Roy Soc Lond Series A Math Phys Sci 1966;260(1109):37–49.